Enhanced Li-Ion Diffusivity of LiFePO$_4$ by Ru Doping: Ab Initio and Machine Learning Force Field Results

Bhubnesh Lama, Alevtina L. Smirnova, and Tula R. Paudel*

Cite This: https://doi.org/10.1021/acsaem.3c01429

Read Online

ACCESS | Metrics & More | Article Recommendations | SI Supporting Information

ABSTRACT: Ionic diffusivity plays a central role in battery performance. A cathode material for lithium-ion (Li-ion) batteries, LiFePO$_4$ (LFP), performs poorly at high current rates due to low Li-ion diffusivity. An increase in ionic diffusivity is essential to enhance battery performance for high-power-density applications such as hybrid and electric vehicles. Here, we use molecular dynamics simulations with machine learning force field and climbing-image nudged elastic band calculations to show that Li-ion diffusivity in LFP increases when doped with the transition-metal dopant ruthenium. This increase is associated with a reduction in Li-diffusion energy barrier, diffusion length, and Li-vacancy formation energy, and it is accompanied by changes in the electronic band structure, specifically the appearance of electronic states in the middle of the band gap and vicinity of the conduction band.

KEYWORDS: LiFePO$_4$, LFP, doping-induced changes in conductivity, ionic diffusivity, nudged elastic band, on-the-fly learning, machine learning force field, molecular dynamics
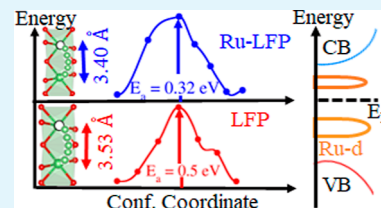
1. INTRODUCTION

LiFePO$_4$ (LFP) is an extensively studied cathode material for large-capacity lithium-ion (Li-ion) batteries needed for electric vehicles and other applications due to its relatively high theoretical specific capacity of 170 mA h g^{-1}, high energy density, chemical and thermal stability, lower cost, environmentally benign nature, and good cyclability.[1−4] It has a cell voltage of 3.5 V[1,5] versus Li$^+$/Li^0. The phases LiFePO$_4$ and FePO$_4$, which form during the intercalation and deintercalation of Li ions, have the same structure and nearly the same volume, leading to excellent electrochemical cyclability and charge retention. However, its practical capacity is low (∼110 mA h g^{-1}) even at low current densities of about 2 mA/g; this capacity decreases further at increased current rates,[1] suggesting limited applicability for both low- and high-power rechargeable batteries. Low values of practical capacity are due to its poor electronic conductivity (∼10^{-9} to 10^{-10} S cm^{-1})[6] and low Li-ion diffusivity (∼10^{-12} to 10^{-14} cm^2 s^{-1}).[5,7−9] The poor ionic diffusivity limits electrochemical performance as evidenced by low power density and low capacity retention during charging/discharging, leading to reduced cycle life and low charge/discharge rates.[5−8,10,11] Increasing the electronic conductivity and Li-ion diffusivity is essential for improving the rate performance of high-power rechargeable batteries.

It is known that local crystal structure, electronic configuration, and ionic diffusion can be enhanced by surface engineering, for example, coating with carbon,[12] minimizing the particle size at the nanoscale, and doping with suitable dopants.[13] The carbon coating[5,14−16] improves the electron conductivity by forming the interparticle charge-conduction layers with enhanced charge mobility. Minimizing particle size

at the nanoscale increases the surface-volume ratio and eases the interparticle transfer of electrons and ions. Doping with suitable dopants increases the electronic conductivity and Li-ion diffusivity by reducing the energy band gap, increasing the charge carrier density, forming new defect states in the bands, shortening the diffusion path, expanding the diffusion channel, and lowering the diffusion activation energy barrier. Changes in the local crystal structures, lattice distortions, and electronic structures accompany these changes.

The literature on the doping of LFP includes primarily experimental studies[6,8,9,17−26] along with few theoretical studies[27−31] including large materials genomics type of study involving multiple dopants.[32] While these studies aim to show that suitable dopants can improve electrochemical performance, a detailed understanding of the effect of doping leading to performance enhancement remains unclear. The first-principles atomistic simulations known for unveiling the structure−composition relationship contribute to the understanding of mechanisms behind performance enhancement by elucidating the effect of dopants on electronic band structure, electrical conductivity, ionic diffusivity, lattice distortion, and average lithium-ion intercalation/deintercalation potential. Since the mechanisms behind enhanced properties for many dopants remain unclear, we chose Ru as a model dopant and

investigated its effect on the local structure and electronic and ionic conduction. While LFP might contain other intrinsic and extrinsic defects and they manifest themselves depending on growth conditions, our calculation focuses on unraveling detailed fundamental reasons behind performance enhancements upon Ru doping, keeping other macroscopic conditions nominally the same. Typically, in intentional doping studies, the concentration of the dopants is high enough to dominate the observed changes in properties.

2. METHODS

2.1. Density Functional Theory Parameters and Structural Details. We used the density functional theory (DFT) implemented in the Vienna ab initio Simulation Package (VASP) within the plane-wave pseudopotential method[33] to evaluate the structure−property relationships of the LFP and Ru-doped LFP. The projected augmented wave[34] method was used to evaluate the electron−ion potential. The Perdew−Burke−Ernzerhof form of spin-polarized generalized gradient approximation (GGA)[35] was used to approximate the exchange−correlation effects. Since the GGA method underestimates the band gap and Li-ion intercalation voltage partly due to incomplete accounting of strong electron correlation within the Fe 3d state, we used the GGA + U method,[36] where Hubbard correction U describes the on-site electron repulsion. We found that the GGA + U method with $U_{eff} = U − J$ of 5 eV at the Fe 3d state (U = 5 eV and J = 0, J is the exchange term), calculated band gap energy, and the average Li intercalation/deintercalation voltage [also known as an open-circuit voltage (OCV)] are close to the experimentally measured values[1,5,37−41] (Table S1). Thus, we adopt a U_{eff} of 5 eV for all calculations. Structure optimizations are performed using a kinetic energy cutoff of 520 eV, a k-point mesh of 2 × 2 × 2, and convergence criteria of energy difference of 10^{-6} eV and atomic force of 0.01 eV $Å^{-1}$. The valence electronic configurations for Li, Fe, P, O and Ru are $1s^2 2s^1$, $3d^7 4s^1$, $3s^2 3p^3$, $2s^2 2p^4$, and $4p^6 5s^1 4d^7$, respectively. The denser k-point mesh of 4 × 3 × 4 is used for calculating the electronic density of states (DOS). We have also used the HSE06 functional[42,43] in our calculations to calculate the DOS for verification of the energy position of the Ru-defect states.

We varied the concentration of dopants using different-sized supercells. We used a 2 × 2 × 1 supercell with one Fe atom replaced with one Ru atom to create $LiFe_{0.94}Ru_{0.06}PO_4$ and a unit cell with one Fe atom replaced with one Ru atom to create $LiFe_{0.75}Ru_{0.25}PO_4$ (Figure S1). The Ru-defect sites were chosen randomly. The distance between doped Ru atoms depends on the concentration. In $LiFe_{0.94}Ru_{0.06}PO_4$, the typical inter-Ru atom distance is 9.5 Å, whereas in the case of $LiFe_{0.75}Ru_{0.25}PO_4$, the inter-Ru atom distance is 4.74 Å. The best electrochemical performance has been observed in $LiFe_{0.93}Ru_{0.07}PO_4$;[44] thus, we have chosen the $LiFe_{0.94}Ru_{0.06}PO_4$ stoichiometry for our study. The conjugate gradient relaxation doped structure with varying concentrations (0.06 to 0.25 atomic %) retains the orthorhombic structure with a lattice constant and volume reported in Table 1 (manuscript).

2.2. Climbing-Image Nudged Elastic Band Method. We used the climbing-image nudged elastic band (CI-NEB) method[45,46] as implemented in the VTST[47] interface to the VASP to calculate the activation energy barrier for Li diffusion along the path that Li-ions follow when hopping between two neighboring Li sites. Five intermediate configurations (also called images) were generated by linear interpolation between the initial and final configurations. The local relaxation calculations using a quick-min[46] force-based optimizer were implemented to find the saddle point (the highest energy image) with the convergence criteria of maximum force of 0.01 eV $Å^{-1}$ on all the images. For these calculations, we used the maximum step size of 0.2Å for the translation of the atom and the dynamical time step of 0.01 fs.

2.3. Ab Initio Molecular Dynamics Machine Learning Force Field Generation. We performed molecular dynamics (MD) simulations using ab initio and machine learning force field (MLFF) with VASP to evaluate the dynamical quantities like mean square displacement (MSD), diffusion coefficient (or diffusivity), and diffusion activation energy barrier.

MLFFs were generated on-the-fly[48,49] during Ab-Initio-MD (AIMD) simulations. In this work, AIMD simulations use the NVT ensemble with the temperature of the system controlled by the Nose−Hoover thermostat[50] with a time step of 1 fs for a duration of 10 ps heated gradually from 800 to 2000 K. The simulation cell consisted of a 2 × 1 × 1 supercell of LFP with 56 atoms (8 formula units). We took a relaxed structure from the static DFT calculations as the initial structure for on-the-fly learning calculations. Only 915 AIMD calculations were performed out of a total of 10,000 MD steps, and the structures corresponding to these AIMD calculations constitute the reference structure data sets. From these reference-structure data sets, 1844, 3104, 8000, 2523, and 828 local reference configurations were selected for Fe, Li, O, P, and Ru, respectively. These local reference configurations describe the local environment of the involved atoms. The total energy of each structure was evaluated as the sum of the local energies that are a function of the local configurations. The local energies were fitted using the kernel regression method[48,51] to generate the force field function. The threshold for the Bayesian error on the forces was set at 0.002 eV/Å, which was set to update automatically as the simulation becomes more accurate with the number of steps.

For constructing the descriptors and kernel functions,[52−54] we set the cutoff radius of 5 Å to represent the local environment of each atom. The width of the Gaussian functions used for broadening the atomic distributions of the descriptors was set to 0.5 Å. We used 8 radial basis functions to construct descriptors. The weight of the radial descriptors in the kernel was chosen as β = 0.1, and the polynomial power of the kernel was set to be ς = 4. The CUR algorithm[54] was used to sparsify local reference configurations with a threshold of 10^{-9}.

To validate the generated MLFF, we plotted the differences between the energies, forces, and stress tensors (Figure S2) predicted by the MLFF and the DFT calculations for the structures in the training data set. We found that the differences in energies, forces, and stress tensors are less than 4 meV $atom^{-1}$, 0.8 eV $Å^{-1}$, and 6 kbar, respectively. The root-mean-square errors in the energies, forces, and stress tensors predicted by this MLFF for the training data set were 1.25 meV $atom^{-1}$, 0.076 eV $Å^{-1}$, and 1.17 kbar, respectively. The zero-temperature lattice parameters and volume for undoped and doped LFP were also calculated using MLFF and compared with the values from the DFT calculations (Table S2). We found the difference in lattice parameters and volumes to be less than 0.5%. These tests and results from the previous literature[48,51,52,55] indicate that the MLFF calculations have an accuracy near the DFT calculations.

2.4. MD Calculations. We performed the MD simulations on both pure and doped LFP 2 × 2 × 1 supercells (112 atoms; 16 formula units) using the MLFF generated during on-the-fly machine learning at various temperatures (1000, 1200, 1400, 1500, 1600, 1700, 1800, and 1900 K) for 40 ps to calculate the MSDs of Li, Fe, P, O, and Ru atoms. We performed the MD simulations at higher temperatures as we did not see significant Li migration even at 1200 K with a simulation time of 40 ps (Figure S3), consistent with the previous AIMD studies.[56,57] Note that the 2 × 2 × 1 supercell is approximately isotropic, which allows the defect-induced charge density to distribute radially around the defect sites.

Table 1. Lattice Parameters and Volume for Pure and Ru-Doped LiFePO4 Using the GGA + U, U = 5 eV Method

lattice parameter	$LiFePO_4$	$LiFe_{0.94}Ru_{0.06}PO_4$	$LiFe_{0.75}Ru_{0.25}PO_4$
a (Å)	4.743	4.745	4.746
b (Å)	6.066	6.060	6.045
c (Å)	10.419	10.405	10.377
volume ($Å^3$)	299.82	299.28	297.78

3. RESULTS AND DISCUSSION

3.1. Site-Selective Doping. The doped Ru prefers to occupy the Fe site. Figure 1a shows the crystal structure of
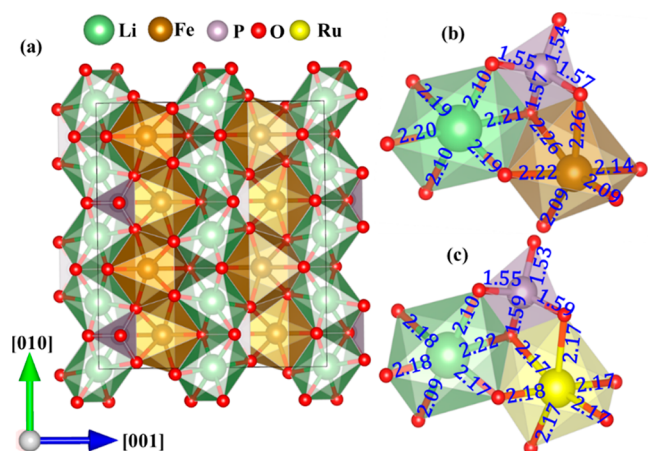

Figure 1. Crystal structure of LiFePO$_4$ (LFP) (a), evolution of Fe- and Li-centered octahedra, and P-centered tetrahedra of pure LFP (b) upon doping with Ru (c).

LiFePO$_4$ with the Fe site located at the center of the O-centric octahedra interspersed between Li-centered octahedra. PO$_4$

tetrahedra fit between tilted Fe-centered and Li-centered octahedra, as shown in Figure 1b. Out of Li, Fe, P, and O and interstitial sites, Ru prefers occupying the Fe site because of relatively similar ionic radii and preference of the Ru ion for an octahedral environment similar to Fe. Table S3 shows the energy cost of replacing Fe, Li, P, and O with Ru and the energy cost associated with occupying interstitial sites. The energy cost for replacing the ions is calculated using $E(\text{HF}) = E(\text{doped}) - E(\text{pure}) \pm \sum_i n_i \mu_i$ where $E(\text{doped})$ and $E(\text{pure})$ are the energies of the doped and pure LiFeO$_4$ and n_i is the number of ions added or removed with the corresponding energy μ_i. The energy cost of replacing Fe is 1.46 eV, which is lower than that of replacing other atoms in the lattice. Below, we discuss the effect of such replacement.

3.2. Effects of Doping on Structure. Ru doping reduces the volume of LFP by asymmetrical change of the lattice parameters. Table 1 summarizes defect-induced changes in the LFP lattice upon Ru-doping. Lattice parameter c decreases upon incorporating Ru, while a and b remain roughly the same, resulting in decreased volumes. A similar decrease in volume upon doping has been observed experimentally.[19,44] This slight reduction has been attributed to the smaller ionic radius of the Ru ion (0.68 Å) compared to that of the Fe ion (0.78 Å), leading to local distortion (Figure 1b,c). The asymmetric reduction in lattice parameters indicates more asymmetric bonding with nearby O, with reduced bond length along the
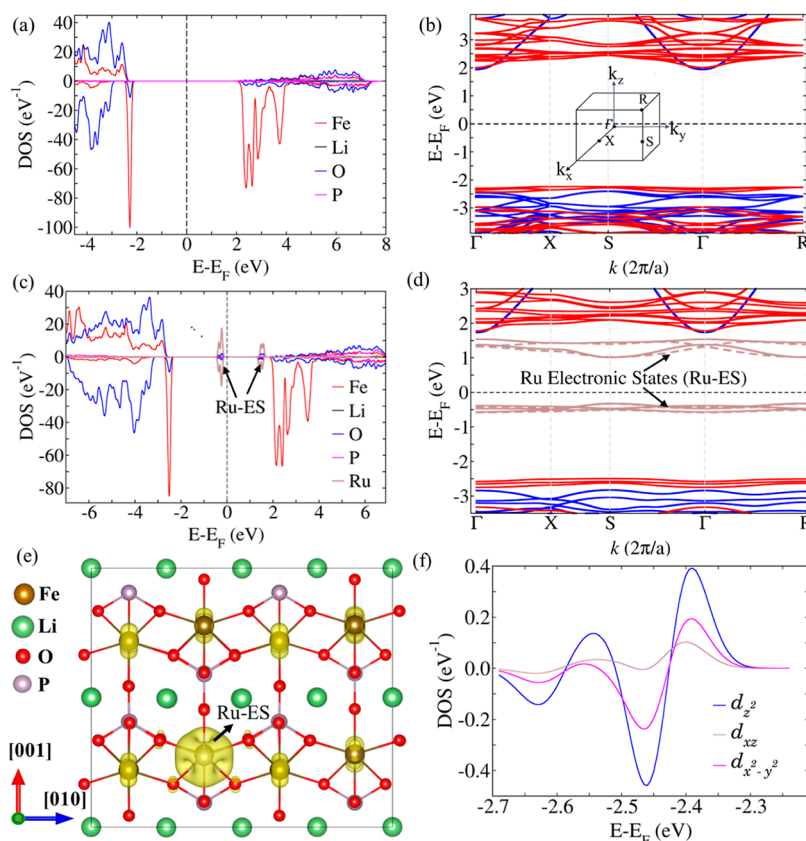

Figure 2. DOS and band structure of LiFePO$_4$ (a,b) and Ru-doped LiFePO$_4$ (c,d), respectively. Blue and red bands in (b,d) represent the spin-up and spin-down bands. The inset in (b) shows the Brillouin zone. The position of Ru electronic states is shown in both DOS and band structure plots. In (d), solid brown lines are for spin-up and broken brown lines are for spin-down bands. Zero of the energy level corresponds to the Fermi energy. The iso-surface plot (e) shows the distribution of charge density induced due to Ru doping with the iso-surface level set to 0.012 e/Å^3. Differential DOS (f) evaluated by taking the difference between the DOS of Fe in pure and doped one, plotted as a function of energy near the VBM edge.

[001] directions compared to others in the FeO_6 octahedron. This effect is mediated by a defect-induced charge distribution in a nearby Fe-site that is oriented along the [001] direction because it is mainly contributed by d_{z^2} and d_{xz} orbitals (Figure 2e,f). Any possible interaction involving these orbitals would likely affect the c-lattice constant more than others.

3.3. Effects of Doping on the Band Structure.

Figure 2 shows that doping Ru induces electronic states that are mostly localized around the defect site and leaves valence and conduction bands roughly unchanged. Figure 2a,c shows the DOS, and Figure 2b,d shows corresponding band structures of pure and Ru-doped LFP showing that Ru-electronic states (gray lines) lie in the band gap. We found that Ru as a dopant is only weakly hybridized, and its electronic configuration remains close to that of Ru solid. The occupied and empty Ru states can be qualitatively interpreted as t_{2g} and e_g orbitals in low spin configurations, occupying about 4.7 electrons per dopant. The availability of these extra electronic charges due to dopants may help in enhancing the specific charge capacity.

The position of the Ru-electronic states was verified with hybrid functional HSE06,[42,43] which explicitly includes the part of the exact Hartree−Fock exchange to account for electronic correlations missing in standard generalized gradient functionals. The DOS calculation using the HSE06 functional (Figure S4) also shows that Ru-electronic states lie in the band gap. The valence band maxima and conduction band minima of the Ru-doped case consist of the Fe-d state like in the undoped case. If the Ru-electronic states are removed from the gap of the doped case, the band structures of pure and doped LFP become roughly similar, except that the conduction bands lie near the Fermi energy level in the doped case.

3.4. Effects of Doping-Induced Charge Distribution and Li-Vacancy Formation.

The lithium vacancy formation energy, $E_v(Li_v) = E(Li_v) − E(Li) + n\mu_{Li}$ where $E(Li_v)$ and $E(Li)$ are the energies of the supercell with and without Li vacancies, n is the number of Li vacancies, and μ_{Li} is the chemical potential of Li, decreases upon Ru-doping as shown in Table 2. Li atoms removed to create vacancies in the

Table 2. Lithium Vacancy Formation Energy for Pure and Doped LFP and the Distance of the Vacant Li Site from the Dopant Ru Atom

	pure	doped LFP			
Li distance from Ru (Å)		3.60	3.70	5.63	5.59
Li vacancy formation energy (eV)	3.83	2.67	2.71	2.72	2.73

supercell are shown in Figure S5. Though the defect-induced charge is mostly localized around the defect sites, it spans approximately 1 nm around the defect (Figure 2e). Since some of the charges moved away from the defect site, the defect site is slightly positively charged. The interaction between an additional positive charge (hole) induced by a Li vacancy and a positively charged atom at the defect site will increase the energy of the defective system and reduce the formation energy of Li-vacancy.

Alternatively, the reduction can be interpreted as Li-vacancy helping to restore charge neutrality that is perturbed by donor-type Ru_{Fe} defects. As a result, the average Li-vacancy formation energy decreases by ∼1 eV (Table 2) in the presence of Ru dopants. As expected, this reduction is dependent upon the distance from the dopant site. The farther the distance from Ru, the lower the reduction in the Li-vacancy formation

energy. This reduction of Li-vacancy formation energy may lead to the reduction of the amount of energy required to charge the battery and, hence, charging voltage.

3.5. Effects of Doping on the Voltage for Li-Ion Intercalation.

The Li intercalation voltage remains roughly the same after doping. The evaluated average Li intercalation voltage of 3.59 V for bulk $LiFePO_4$ changes to 3.52 V upon doping; a small change between the two cases lies within the accuracy of the calculations. Li intercalation voltage, also known as OCV, is defined as $V(x) = −[\mu_{Li}^{cathode}(x) − \mu_{Li}^{anode}]/ze$, where z is the number of electrons (e) transferred and $\mu_{Li}^{cathode}$ and μ_{Li}^{anode} are the chemical potentials of the cathode and anode. However, it is convenient to evaluate OCV by evaluating the energy involved in the Li-ion intercalation in the cathode of the cell:[58−62]

$Li_m(cathode) + (n − m)Li = Li_n(cathode)$, the average Li-ion intercalation voltage can be obtained from the ground-state energies calculated from the DFT as $V(x) = −[E_{Li(n)}(cathode) − (n − m)(E_{Li} + E_{Li(m)}(cathode))]/(n − m)e$, where $E_{Li(n)}(cathode)$ and $E_{Li(m)}(cathode)$ are the energy of the cathode having n and m number of Li atoms, E_{Li} is the energy of the isolated Li atom, and $(n − m)$ is the number of Li atoms intercalated in the cathode. In the limit case of $m = 0$, $n = 1$, which corresponds to a fully lithiated/delithiated case, the average Li intercalation voltage of undoped and doped LFP is found to be 3.59 and 3.52 V, respectively. The evaluated average Li intercalation voltage is similar to the experimental value[1,37] of 3.40−3.50 V and the value of 3.46 V evaluated using HSE functionals.

3.6. Doping Induced Modulation of the Li-Ion Activation Barrier.

Doping modulates the ionic conductivity and diffusivity by changing the height of the hopping barrier.

3.6.1. Hopping Barrier Height.

We found that Ru doping reduces the hopping barrier height for Li-ion diffusion. Hopping barrier height is the amount of energy required for the ions to hop from one lattice site to another. It is estimated as the difference between the energy of structures with Li at the saddle point along the hooping path and the energy of the structure with Li at the initial high symmetry position. Figure 3a with one Li vacancy at the center of Li−O octahedra (better seen in Figure 3b) represents the initial minimum energy structure, and Figure 3b with Li at the intermediate sites represents structures at the saddle points. Figure 3b shows 1D chains of Li-centered, lithium−oxygen octahedra extending along the [010] direction with the inter-Li atom distance of 3.03 Å. On the other hand, phosphorus−oxygen tetrahedra exist between two Li−O octahedral chains along the [100] direction with an interlithium distance of 4.74 Å (Figure S6). The Li−O octahedra share their edges and corners along [010], making it possible for bond-to-bond hopping, while in the other directions, these octahedra are separated by P−O tetrahedra and Fe−O octahedra. Figure 3c,d shows the hopping barrier evaluated using CI-NEB methods along the [010] and [100] directions. The evaluated barrier height of 0.5 eV along the [010] direction is significantly smaller than that of 2.5 eV along the [100] direction. Previous calculations[28,57,63−67] have reported similar values for the energy barriers. The even larger barrier height is expected for hopping along the [101] direction owing to the larger separation of 5.72 Å and the presence of Fe−O octahedra between two Li−O octahedral chains.

Ru doping does not break existing chains along [010], and hence, the activation energy remains lower. However, the value
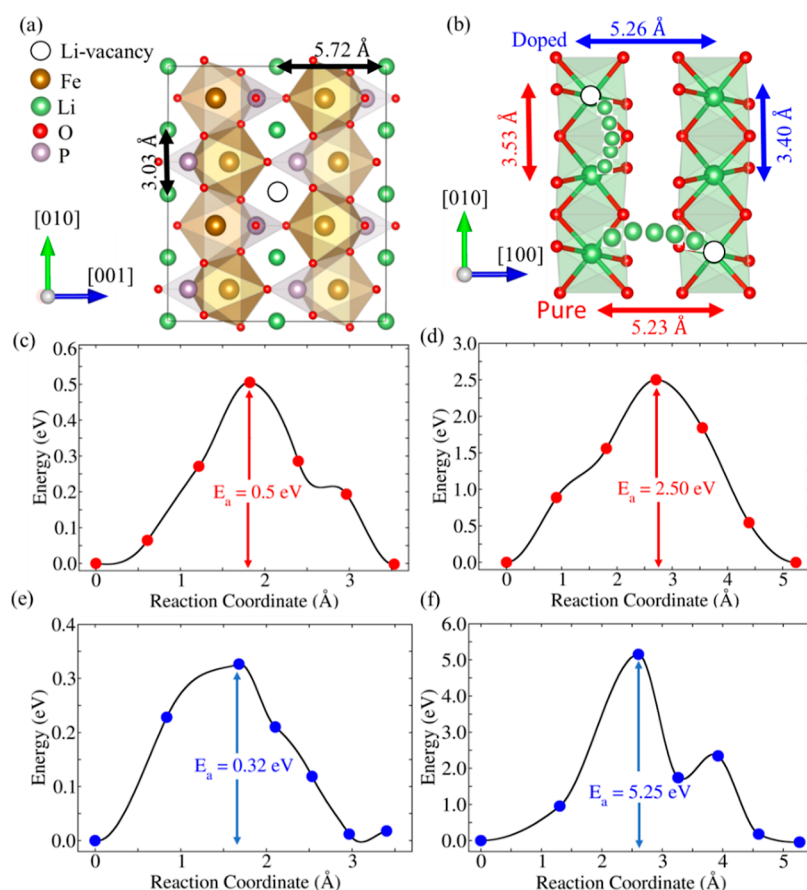
Figure 3. LiFePO$_4$ structure showing iron atoms in the center of the octahedra and lithium vacancy. The distances between lithium atoms are shown along [010] and [100] directions (a). Two Li-centered octahedral chains (b) with the evaluated hopping lengths represented by red and blue double-side red arrows for the pure and doped cases, respectively. Diffusion activation energy along [010] and [100] directions for pure LiFePO$_4$ (c,d) and Ru-doped LiFePO$_4$ (e,f), respectively. In the diffusion activation energy plots, the dots represent the evaluated energy of different configurations with the Li-position shown in (b); solid lines are the spline fit of the calculated energy points; E_a energy of the system with maximum energy.

of the activation energy barrier decreases from 0.5 to 0.32 eV along the [010] direction upon doping. This is consistent with reduced hopping length from 3.53 to 3.40 Å upon doping and reduced Li-vacancy formation energy. The hopping involves moving along the depression of the potential energy landscape, and hopping length does not correspond to the bond length. The hope length, however, increases along the [100] direction, and with it, the activation energy barrier also increases from 2.5 to 5.25 eV.

3.6.2. Li-Ion Diffusivity and Ionic Conductivity. Ruthenium doping enhances diffusivity along the [010] directions due to a reduced activation energy barrier. The diffusivity increases to 3.86×10^{-9} cm^2 s^{-1} from 3.66×10^{-12} along the [010] direction. In contrast to the earlier DFT evaluated value[66] of 10^{-8} cm^2 s^{-1}, our calculated Li-ion diffusivity of 3.66×10^{-12} cm^2 s^{-1} in undoped LiFePO$_4$ at 300 K is comparable to the experimentally calculated values of $\sim10^{-12}$ to 10^{-14} cm^2 s^{-1}.[5,7−9] In this study, the Li-ion diffusion coefficient (or diffusivity) was estimated using the following equation: $D = a^2 \nu \exp\left(-\frac{E_a}{k_B T}\right)$ where a is the Li hopping distance along the diffusion path, ν is the frequency in the range of phonon frequency ($\nu = 10^{12}$ Hz), k_B is the Boltzmann constant, and T is the temperature. As expected from large activation energy barriers, the diffusivity, 2.7×10^{-45} cm^2 s^{-1} for pure and

5.87×10^{-89} cm^2 s^{-1} when doped, along the [100]direction is much smaller than the diffusivity along the [010] direction. This result indicates unidirectional Li diffusion in both pure and doped cases.

The ionic conductivity was further evaluated using the following equation: $\sigma = q^2 N D / V k_B T$, where D is the diffusivity, T is the temperature (K), N/V is the density of ions, and k_B is the Boltzmann constant.[68] It was found that the ionic conductivity increases with doping, as stipulated by D. Specifically, σ increased by 3 orders of magnitude from 3.0×10^{-7} to 3.2×10^{-4} S cm^{-1} along the [010] direction, while the ionic conductivity in the other direction was negligible (10^{33} times smaller). The unidirectional nature of Li-ion diffusivity and the corresponding ionic conductivity in undoped LFP has been noted in previous studies.[28,57,63−67]

3.7. Doping Induced Modification on Atomic Dynamics. Unconstrained finite temperature MD calculations confirm that upon doping, the activation energy barrier for lithium-ion diffusion is decreased, causing enhancement of the ionic diffusivity and conductivity.

Unlike the NEB calculations, where the initial and final geometries are assumed a priori, MD simulations allow unconstrained diffusion of ions according to thermal energy. Figure 4a compares the MSD, MSD$=\frac{1}{N}\sum_{i=1}^{N}|\mathbf{r}_i(t) - \mathbf{r}_i(0)|^2$ where $\mathbf{r}_i(t)$ and $\mathbf{r}_i(0)$ are the position vector of the ion i at time
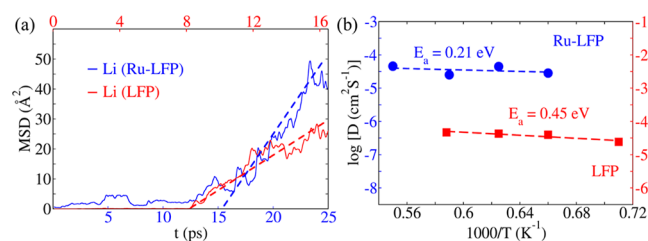
Figure 4. MSD of Li-ions with time along the [010] direction at 1500 K (a) and Arrhenius plot (Li-ion diffusivity vs inverse temperature) along the same direction (b) for pure and Ru-doped LFP with their respective Li-ion diffusion activation energy (E_a). In (a,b), axes for doped and pure LFP are presented in blue and red colors.

t and $t = 0$, respectively, and N is the total number of ions, as a function of time along the [010] direction at 1500 K. As expected, we found that the Li-ions have the largest MSD compared to other ions (Fe, P, O, and Ru) in both doped and pure cases (Figure S7). These suggest that the Li ions diffuse easily during Li intercalation/(deintercalation) through the channels shown in Figure 3a, while the other ions with low MSD maintain structural framework and volume during charging and discharging.

MSD is directly related to the diffusivity as $D = \frac{1}{2}\lim_{t\to\infty}\frac{d}{dt}(\text{MSD}) = \frac{1}{2}$ slope of MSD. We linear fit the MSD vs simulation time (t) data to evaluate the slope.[69,70] During fitting, we only take points that show significant Li-ion diffusion. Figure 4b compares Li-ion diffusivity, a thermally activated process, for doped and undoped LFP as a function of temperature along the [010] direction. The direction is determined by changing position vector **r** of the ions. Figure 4b also shows a linear fit to log D vs $1/T$ data to find the activation energy (E_a), according to Arrhenius expression $D = D_0 \exp\left(-\frac{E_a}{K_B T}\right)$. The calculated values of the activation energy for Li-ion diffusion along [010] for pure, $E_a = 0.45$ eV, and doped, $E_a = 0.21$ eV, LFP were similar to the values obtained from the CI-NEB calculations (Figure 3b,c). The estimated values of the activation energy (E_a) allow us to estimate diffusivity at any temperature, for instance, at room temperature (RT). The evaluated Li ion diffusivity values of 2.79×10^{-11} and 4.15×10^{-8} cm^2 s^{-1} at RT are comparable with the values obtained from our CI-NEB calculations. As expected from MSD results, the diffusivity in the doped case is much larger, by about 3 orders of magnitude than in the undoped case, which is similar to the increase obtained from our CI-NEB calculations. Not surprisingly, the activation energy is much larger and the diffusivity is much smaller in [100] directions. Figure S8 shows Arrhenius plots for pure and doped LFP and their corresponding activation energies (1.62 and 3.08 eV) as well as Li-ion diffusivities (6.03×10^{-29} and 5.84×10^{-49} cm^2 s^{-1}).

4. CONCLUSIONS

In this study, both the CI-NEB calculations and MD simulations show that the Li-ion diffusivity of LFP increases after doping with Ru because of the shortened diffusion path and reduced activation energy accompanied by the reduction of the unit-cell volume. Our energy calculation shows that Ru prefers to occupy Fe sites on doping. Since Ru has slightly smaller ionic radii than that of Fe, the presence of Ru leads to local distortion, resulting in asymmetric reduction in lattice

parameters and decreased volume. Additionally, the calculated electronic structures show that in both undoped and doped LFP cases, the band edges are similar. Still, the doped case has Ru-induced electronic states in the band gap, introducing as much as 4.7 e/dopant, and the availability of extra electrons due to the dopant may help in enhancing the specific charge density. The charges due to defect states are localized around these defects and may not change the electronic conductivity of LFP. Other methods, including coating LFP with conducting materials, may be needed to increase the electronic conductivity of LFP. Thus, our study on doping LFP emphasizes the importance of atomic-level doping for increasing the lithium-ion diffusivity, which may lead to increased power density, maintaining the Li intercalation potential to retain the energy density and electronically conducting coating for enhancing electronic conductivity to improve the overall electrochemical performance of LFP.

■ ASSOCIATED CONTENT

Ⓢ Supporting Information

The Supporting Information is available free of charge at https://pubs.acs.org/doi/10.1021/acsaem.3c01429.

Comparison of the band gap and OCV evaluated using different U_{eff} with experiment; comparison of lattice parameters and volume of doped and undoped LFP; formation energy of Ru doping at different sites; crystal structure showing Ru distribution in LFP, validating MLFFs, MSDs at 1200 K; defect states; positions of Li vacancies; crystal structures of LFP; MSD of ions at 1500 K; and Arrhenius plot of LFP and Ru-LFP (PDF)

■ AUTHOR INFORMATION

Corresponding Author

Tula R. Paudel − *Department of Physics, South Dakota School of Mines and Technology, Rapid City, South Dakota 57701, United States;* ⓞ orcid.org/0000-0002-9952-9435; Email: tula.paudel@sdsmt.edu

Authors

Bhubnesh Lama − *Department of Physics, South Dakota School of Mines and Technology, Rapid City, South Dakota 57701, United States*

Alevtina L. Smirnova − *Department of Chemistry, Biology, and Health Sciences, South Dakota School of Mines and Technology, Rapid City, South Dakota 57701, United States;* ⓞ orcid.org/0000-0003-1520-0331

Complete contact information is available at:
https://pubs.acs.org/10.1021/acsaem.3c01429

Notes

The authors declare no competing financial interest.

Performance Computing Center at South Dakota State University.

■ REFERENCES

(1) Padhi, A. K.; Nanjundaswamy, K. S.; Goodenough, J. B. Phospho-olivines as Positive-Electrode Materials for Rechargeable Lithium Batteries. *J. Electrochem. Soc.* **1997**, *144* (4), 1188−1194.

(2) Ellis, B. L.; Lee, K. T.; Nazar, L. F. Positive Electrode Materials for Li-Ion and Li-Batteries. *Chem. Mater.* **2010**, *22* (3), 691−714.

(3) Prosini, P. P.; Zane, D.; Pasquali, M. Improved Electrochemical Performance of a LiFePO4-Based Composite Cathode. *Electrochim. Acta* **2001**, *46* (23), 3517−3523.

(4) Huang, H.; Yin, S.-C.; Nazar, L. F. Approaching Theoretical Capacity of LiFePO[sub 4] at Room Temperature at High Rates. *Electrochem. Solid-State Lett.* **2001**, *4* (10), A170.

(5) Franger, S.; Le Cras, F.; Bourbon, C.; Rouault, H. LiFePO[Sub 4] Synthesis Routes for Enhanced Electrochemical Performance. *Electrochem. Solid-State Lett.* **2002**, *5* (10), A231.

(6) Chung, S.-Y.; Bloking, J. T.; Chiang, Y.-M. Electronically Conductive Phospho-Olivines as Lithium Storage Electrodes. *Nat. Mater.* **2002**, *1* (2), 123−128.

(7) Prosini, P. Determination of the Chemical Diffusion Coefficient of Lithium in LiFePO4. *Solid State Ionics* **2002**, *148* (1−2), 45−51.

(8) Zhang, B.; Ma, X.; Hou, W.; Yuan, W.; He, L.; Yang, O.; Liu, Y.; Wang, J.; Xu, Y. Revealing the Ultrahigh Rate Performance of the La and Ce Co-Doping LiFePO 4 Composite. *ACS Appl. Energy Mater.* **2022**, *5* (12), 14712−14719.

(9) Gao, Y.; Xiong, K.; Zhang, H.; Zhu, B. Effect of Ru Doping on the Properties of LiFePO4/C Cathode Materials for Lithium-Ion Batteries. *ACS Omega* **2021**, *6* (22), 14122−14129.

(10) Gao, F.; Tang, Z. Kinetic Behavior of LiFePO4/C Cathode Material for Lithium-Ion Batteries. *Electrochim. Acta* **2008**, *53* (15), 5071−5075.

(11) Zhang, B.; Xu, Y.; Wang, J.; Lin, J.; Wang, C.; Chen, Y. Lanthanum and Cerium Co-Doped LiFePO4: Morphology, Electrochemical Performance and Kinetic Study from −30 - + 50 °C. *Electrochim. Acta* **2019**, *322*, 134686.

(12) Kharel, P.; Lama, B.; Flesche, M.; Mehlberg, Z.; Lamsal, B.; Valloppilly, S.; Zhou, Y.; Sellmyer, D. J.; Paudel, T. R. Modifying Magnetic Properties of MnBi with Carbon: An Experimental and Theoretical Study. *J. Phys. D Appl. Phys.* **2022**, *55* (26), 265003.

(13) Paudel, T. R.; Lama, B.; Kharel, P. Ab Initio Study of Alloying of MnBi to Enhance the Energy Product. *RSC Adv.* **2021**, *11* (49), 30955−30960.

(14) Hong, S.-A.; Kim, S. J.; Kim, J.; Lee, B. G.; Chung, K. Y.; Lee, Y.-W. Carbon Coating on Lithium Iron Phosphate (LiFePO4): Comparison between Continuous Supercritical Hydrothermal Method and Solid-State Method. *Chem. Eng. J.* **2012**, *198−199*, 318−326.

(15) Hwang, J.; Kong, K. C.; Chang, W.; Jo, E.; Nam, K.; Kim, J. New Liquid Carbon Dioxide Based Strategy for High Energy/Power Density LiFePO4. *Nano Energy* **2017**, *36*, 398−410.

(16) Zhu, C.; Yu, Y.; Gu, L.; Weichert, K.; Maier, J. Electrospinning of Highly Electroactive Carbon-Coated Single-Crystalline LiFePO4 Nanowires. *Angew. Chem., Int. Ed.* **2011**, *50* (28), 6278−6282.

(17) Gao, L.; Xu, Z.; Zhang, S.; Xu, J.; Tang, K. Enhanced Electrochemical Properties of LiFePO4 Cathode Materials by Co and Zr Multi-Doping. *Solid State Ionics* **2017**, *305* (January), 52−56.

(18) Ban, C.; Yin, W. J.; Tang, H.; Wei, S. H.; Yan, Y.; Dillon, A. C. A Novel Codoping Approach for Enhancing the Performance of LiFePo 4 Cathodes. *Adv. Energy Mater.* **2012**, *2* (8), 1028−1032.

(19) Wang, Y.; Yang, Y.; Hu, X.; Yang, Y.; Shao, H. Electrochemical Performance of Ru-Doped LiFePO4/C Cathode Material for Lithium-Ion Batteries. *J. Alloys Compd.* **2009**, *481* (1−2), 590−594.

(20) Shin, H. C.; Park, S. B.; Jang, H.; Chung, K. Y.; Cho, W. I.; Kim, C. S.; Cho, B. W. Rate Performance and Structural Change of Cr-Doped LiFePO4/C during Cycling. *Electrochim. Acta* **2008**, *53* (27), 7946−7951.

(21) Liu, Y.; Gu, Y. J.; Luo, G. Y.; Chen, Z. L.; Wu, F. Z.; Dai, X. Y.; Mai, Y.; Li, J. Q. Ni-Doped LiFePO4/C as High-Performance Cathode Composites for Li-Ion Batteries. *Ceram. Int.* **2020**, *46* (10), 14857−14863.

(22) Liu, H.; Cao, Q.; Fu, L. J.; Li, C.; Wu, Y. P.; Wu, H. Q. Doping Effects of Zinc on LiFePO4 Cathode Material for Lithium Ion Batteries. *Electrochem. Commun.* **2006**, *8* (10), 1553−1557.

(23) Shenouda, A. Y.; Liu, H. K. Studies on Electrochemical Behaviour of Zinc-Doped LiFePO4 for Lithium Battery Positive Electrode. *J. Alloys Compd.* **2009**, *477* (1−2), 498−503.

(24) Zhao, N.; Li, Y.; Zhi, X.; Wang, L.; Zhao, X.; Wang, Y.; Liang, G. Effect of Ce3+ Doping on the Properties of LiFePO4 Cathode Material. *J. Rare Earths* **2016**, *34* (2), 174−180.

(25) Okada, K.; Kimura, I.; Machida, K. High Rate Capability by Sulfur-Doping into LiFePO 4 Matrix. *RSC Adv.* **2018**, *8* (11), 5848−5853.

(26) Liu, Y.; Qin, W.; Zhang, D.; Feng, L.; Wu, L. Effect of Na+ in Situ Doping on LiFePO4/C Cathode Material for Lithium-Ion Batteries. *Prog. Nat. Sci.: Mater. Int.* **2021**, *31* (1), 14−18.

(27) Hoang, K.; Johannes, M. Tailoring Native Defects in LiFePO4: Insights from First-Principles Calculations. *Chem. Mater.* **2011**, *23* (11), 3003−3013.

(28) Islam, M. S.; Driscoll, D. J.; Fisher, C. A. J.; Slater, P. R. Atomic-Scale Investigation of Defects, Dopants, and Lithium Transport in the LiFePO 4 Olivine-Type Battery Material. *Chem. Mater.* **2005**, *17* (20), 5085−5092.

(29) Malik, R.; Burch, D.; Bazant, M.; Ceder, G. Particle Size Dependence of the Ionic Diffusivity. *Nano Lett.* **2010**, *10* (10), 4123−4127.

(30) Fisher, C. A. J.; Hart Prieto, V. M.; Islam, M. S. Lithium Battery Materials LiMPO4 (M = Mn, Fe, Co, and Ni): Insights into Defect Association, Transport Mechanisms, and Doping Behavior. *Chem. Mater.* **2008**, *20* (18), 5907−5915.

(31) Karimzadeh, S.; Safaei, B.; Huang, W.; Jen, T.-C. Theoretical Investigation on Niobium Doped LiFePO4 Cathode Material for High Performance Lithium-Ion Batteries. *J. Energy Storage* **2023**, *67* (April), 107572.

(32) Zhang, B.; He, Y.; Gao, H.; Wang, X.; Liu, J.; Xu, H.; Wang, L.; He, X. Unraveling the Doping Mechanisms in Lithium Iron Phosphate. *Energy Mater.* **2022**, *2* (2), 200013.

(33) Kresse, G.; Furthmüller, J. Efficient Iterative Schemes for Ab Initio Total-Energy Calculations Using a Plane-Wave Basis Set. *Phys. Rev. B: Condens. Matter Mater. Phys.* **1996**, *54* (16), 11169−11186.

(34) Blöchl, P. E. Projector Augmented-Wave Method. *Phys. Rev. B: Condens. Matter Mater. Phys.* **1994**, *50* (24), 17953−17979.

(35) Perdew, J. P.; Burke, K.; Ernzerhof, M. Generalized Gradient Approximation Made Simple. *Phys. Rev. Lett.* **1996**, *77* (18), 3865−3868.

(36) Dudarev, S.; Botton, G.; Savrasov, S. Y.; Humphreys, C. J.; Sutton, A. P. Electron-Energy-Loss Spectra and the Structural Stability of Nickel Oxide: An LSDA+U Study. *Phys. Rev. B: Condens. Matter Mater. Phys.* **1998**, *57* (3), 1505−1509.

(37) Yamada, A.; Chung, S. C.; Hinokuma, K. Optimized LiFePO[Sub 4] for Lithium Battery Cathodes. *J. Electrochem. Soc.* **2001**, *148* (3), A224.

(38) Zhou, F.; Kang, K.; Maxisch, T.; Ceder, G.; Morgan, D. The Electronic Structure and Band Gap of LiFePO4 and LiMnPO 4. *Solid State Commun.* **2004**, *132* (3−4), 181−186.

(39) Zaghib, K.; Mauger, A.; Goodenough, J. B.; Gendron, F.; Julien, C. M. Electronic, Optical, and Magnetic Properties of LiFePO 4: Small Magnetic Polaron Effects. *Chem. Mater.* **2007**, *19* (15), 3740−3747.

(40) Augustsson, A.; Zhuang, G. V.; Butorin, S. M.; Osorio-Guillén, J. M.; Dong, C. L.; Ahuja, R.; Chang, C. L.; Ross, P. N.; Nordgren, J.; Guo, J.-H. Electronic structure of phospho-olivines LixFePO4(x=,1) from soft-x-ray-absorption and -emission spectroscopies. *J. Chem. Phys.* **2005**, *123* (18), 184717.

(41) Furutsuki, S.; Chung, S.-C.; Nishimura, S.; Kudo, Y.; Yamashita, K.; Yamada, A. Electrochromism of Li$_x$FePO$_4$ Induced by Intervalence Charge Transfer Transition. *J. Phys. Chem. C* **2012**, *116* (29), 15259−15264.

(42) Heyd, J.; Scuseria, G. E.; Ernzerhof, M. Hybrid Functionals Based on a Screened Coulomb Potential. *J. Chem. Phys.* **2003**, *118* (18), 8207−8215.

(43) Heyd, J.; Scuseria, G. E.; Ernzerhof, M. Erratum: "Hybrid functionals based on a screened Coulomb potential" [J. Chem. Phys. 118, 8207 (2003)]. *J. Chem. Phys.* **2006**, *124*, 219906.

(44) Yolun, A.; Altin, E.; Altundag, S.; Arshad, M.; Abbas, S. M.; Altin, S. Investigation of Structural and Electrochemical Performance of Ru-Substituted LiFePO4 Cathode Material: An Improvement of the Capacity and Rate Performance. *J. Mater. Sci.: Mater. Electron.* **2022**, *33* (9), 6670−6680.

(45) Henkelman, G.; Uberuaga, B. P.; Jónsson, H. A Climbing Image Nudged Elastic Band Method for Finding Saddle Points and Minimum Energy Paths. *J. Chem. Phys.* **2000**, *113* (22), 9901−9904.

(46) Sheppard, D.; Terrell, R.; Henkelman, G. Optimization Methods for Finding Minimum Energy Paths. *J. Chem. Phys.* **2008**, *128* (13), 134106.

(47) VTST Tools Home page. http://theory.cm.utexas.edu/vtsttools/ (accessed August 08, 2023).

(48) Jinnouchi, R.; Karsai, F.; Kresse, G. On-the-Fly Machine Learning Force Field Generation: Application to Melting Points. *Phys. Rev. B* **2019**, *100* (1), 014105−014109.

(49) Jinnouchi, R.; Lahnsteiner, J.; Karsai, F.; Kresse, G.; Bokdam, M. Phase Transitions of Hybrid Perovskites Simulated by Machine-Learning Force Fields Trained on the Fly with Bayesian Inference. *Phys. Rev. Lett.* **2019**, *122* (22), 225701.

(50) Nosé, S. A Unified Formulation of the Constant Temperature Molecular Dynamics Methods. *J. Chem. Phys.* **1984**, *81* (1), 511−519.

(51) Verdi, C.; Karsai, F.; Liu, P.; Jinnouchi, R.; Kresse, G. Thermal Transport and Phase Transitions of Zirconia by On-the-Fly Machine-Learned Interatomic Potentials. *npj Comput. Mater.* **2021**, *7* (1), 156.

(52) Behler, J. Perspective: Machine Learning Potentials for Atomistic Simulations. *J. Chem. Phys.* **2016**, *145* (17), 170901.

(53) Podryabinkin, E. V.; Shapeev, A. V. Active Learning of Linearly Parametrized Interatomic Potentials. *Comput. Mater. Sci.* **2017**, *140*, 171−180.

(54) Jinnouchi, R.; Karsai, F.; Verdi, C.; Asahi, R.; Kresse, G. Descriptors Representing Two- and Three-Body Atomic Distributions and Their Effects on the Accuracy of Machine-Learned Inter-Atomic Potentials. *J. Chem. Phys.* **2020**, *152* (23), 234102.

(55) Bartók, A. P.; De, S.; Poelking, C.; Bernstein, N.; Kermode, J. R.; Csányi, G.; Ceriotti, M. Machine Learning Unifies the Modeling of Materials and Molecules. *Sci. Adv.* **2017**, *3* (12), No. e1701816.

(56) Yang, J.; Tse, J. S. Li Ion Diffusion Mechanisms in LiFePO 4 : An Ab Initio Molecular Dynamics Study. *J. Phys. Chem. A* **2011**, *115* (45), 13045−13049.

(57) Ouyang, C.; Shi, S.; Wang, Z.; Huang, X.; Chen, L. First-Principles Study of Li Ion Diffusion in LiFePO4. *Phys. Rev. B: Condens. Matter Mater. Phys.* **2004**, *69* (10), 104303.

(58) Aydinol, M.; Kohan, A.; Ceder, G.; Cho, K.; Joannopoulos, J. Ab Initio Study of Lithium Intercalation in Metal Oxides and Metal Dichalcogenides. *Phys. Rev. B: Condens. Matter Mater. Phys.* **1997**, *56* (3), 1354−1365.

(59) Aydinol, M. K.; Ceder, G. First-Principles Prediction of Insertion Potentials in Li-Mn Oxides for Secondary Li Batteries. *J. Electrochem. Soc.* **1997**, *144* (11), 3832−3835.

(60) Aydinol, M. K.; Kohan, A. F.; Ceder, G. Ab Initio Calculation of the Intercalation Voltage of Lithium-Transition-Metal Oxide Electrodes for Rechargeable Batteries. *J. Power Sources* **1997**, *68* (2), 664−668.

(61) Zhou, F.; Cococcioni, M.; Marianetti, C. A.; Morgan, D.; Ceder, G. First-Principles Prediction of Redox Potentials in Transition-Metal Compounds with LDA + U. *Phys. Rev. B: Condens. Matter Mater. Phys.* **2004**, *70* (23), 235121−235128.

(62) Arroyo-de Dompablo, M. E.; Armand, M.; Tarascon, J. M.; Amador, U. On-Demand Design of Polyoxianionic Cathode Materials Based on Electronegativity Correlations: An Exploration of the Li2MSiO4 System (M = Fe, Mn, Co, Ni). *Electrochem. Commun.* **2006**, *8* (8), 1292−1298.

(63) Hu, B.; Tao, G. Molecular Dynamics Simulations on Lithium Diffusion in LiFePO4: The Effect of Anti-Site Defects. *J. Mater. Chem. A* **2015**, *3* (40), 20399−20407.

(64) Kutteh, R.; Avdeev, M. Initial Assessment of an Empirical Potential as a Portable Tool for Rapid Investigation of Li + Diffusion in Li + -Battery Cathode Materials. *J. Phys. Chem. C* **2014**, *118* (21), 11203−11214.

(65) Kuss, C.; Liang, G.; Schougaard, S. B. Atomistic Modeling of Site Exchange Defects in Lithium Iron Phosphate and Iron Phosphate. *J. Mater. Chem.* **2012**, *22* (47), 24889−24893.

(66) Morgan, D.; Van der Ven, A.; Ceder, G. Li Conductivity in Li[sub x]MPO[sub 4] (M = Mn, Fe, Co, Ni) Olivine Materials. *Electrochem. Solid-State Lett.* **2004**, *7* (2), A30.

(67) Dai, K.; Gu, F.; Wang, Q.; Shui, M. The New Insight into the Lithium Migration Mechanism of LiFePO4 by Atomic Simulation Method. *Ionics* **2021**, *27* (4), 1477−1490.

(68) Heenen, H. H.; Voss, J.; Scheurer, C.; Reuter, K.; Luntz, A. C. Multi-Ion Conduction in Li 3 OCl Glass Electrolytes. *J. Phys. Chem. Lett.* **2019**, *10* (9), 2264−2269.

(69) Xu, Z.; Duan, H.; Dou, Z.; Zheng, M.; Lin, Y.; Xia, Y.; Zhao, H.; Xia, Y. Machine Learning Molecular Dynamics Simulation Identifying Weakly Negative Effect of Polyanion Rotation on Li-Ion Migration. *npj Comput. Mater.* **2023**, *9* (1), 105.

(70) Yang, Y.; Zhu, H. Effects of F and Cl Doping in Cubic Li7La3Zr2O12Solid Electrolyte: A First-Principles Investigation. *ACS Appl. Energy Mater.* **2022**, *5* (12), 15086−15092.